Journal of Power Sources 196 (2011) 9672–9681

Contents lists available at ScienceDirect

Journal of Power Sources

journal homepage: www.elsevier.com/locate/jpowsour

Effects of electrode particle morphology on stress generation in silicon during lithium insertion

Christopher M. DeLuca[a], Kurt Maute[a,*], Martin L. Dunn[b]

[a] Department of Aerospace Science and Engineering, University of Colorado at Boulder, Boulder, CO 80309, United States
[b] Department of Mechanical Engineering, University of Colorado at Boulder, Boulder, CO 80309, United States

ARTICLE INFO

Article history:
Received 28 March 2011
Received in revised form 8 July 2011
Accepted 8 July 2011
Available online 2 August 2011

Keywords:
Lithium ion battery
Electrode design
Particle morphology
Stress-diffusion coupling
Butler–Volmer model

ABSTRACT

We study the effects of particle morphology and size on stress generation during Li insertion into Si particles using a fully coupled diffusion-elasticity model implemented in a finite element formulation. The model includes electrochemical reaction kinetics through a Butler–Volmer equation, concentration-dependent material properties, and surface elasticity. Focusing on two idealized geometries (hollow spheres and cylinders), we simulate stresses during Li insertion in Si. These systems describe a wide variety of morphologies that have been fabricated and studied experimentally, including particles, nanowires, nanotubes, and porous solids. We find that stresses generated in solid particles during Li insertion decrease as particle radii decrease from μm-scale, but reach a minimum at about 150 nm. Surface stresses then begin to dominate the stress states as the particle size continues to decrease. The minimum occurs at larger radii for hollow particles. We also find that hollow particles experience lower stresses than solid ones, but our results suggest that there is not a significant difference in maximum stress magnitudes for spherical and cylindrical particles. Studying the influence of concentration-dependent elastic moduli we find that while they can significantly influence stress generation for potentiostatic insertion, their role is minimal when surface reaction kinetics are considered.

1. Introduction

There is an increasing awareness that mechanical effects play significant roles in the performance and lifetime of rechargeable lithium ion batteries. Mechanical effects primarily arise from the deformation that occurs when Li ions are inserted into and extracted from active hosts in battery electrodes. Battery electrodes are typically heterogeneous materials consisting of an active material (∼80% by mass) held together by a binder (∼10% by mass) doped with a conductive additive (∼10% by mass). In addition to these composite electrodes that essentially consist of a random aggregate of active particles, micro and nanofabrication technologies are being widely used to fabricate ordered arrays of active materials for electrodes [1–4]. In the cathode, metal oxides are the active material of choice and in the anode carbonaceous materials are most commonly used. Electrochemical surface reactions generate a flux of Li ions that diffuse into the active particles, resulting in deformation of the particle. The associated volume changes can range from a few to a few hundred percent depending on the materials used. Volume changes can lead to cracking of the electrode and the particles themselves, as well as debonding of the particles from the binder. This can result in electrical disconnects that render portions of the active material incapable of participating in Li storage which is manifested as capacity fade during cycling.

Today, at least three areas of research are actively pursued that are related to mechanical effects: (i) the development and use of new active materials, (ii) making particles in the nanometer scale, and (iii) making particles with different morphologies. These all impact the amount and type of deformation that can occur during Li insertion as well as the resulting stresses that can drive mechanical degradation. Although these research areas are not necessarily being pursued just to address mechanical phenomena, they all play an interesting role.

An especially exciting pursuit is the use of silicon as an active material for anodes because it exhibits the highest known capacity (>4000 mAh g^{-1} compared to ∼372 mAh g^{-1} for carbon) [5,6]. This high capacity comes with the challenge that Si expands about 300–400% [1,7] during Li insertion; at full saturation each Si atom accommodates 4.4 Li atoms [8,9]. The strain associated with Li insertion is typically non-uniform through a particle and as such results in stresses that can crack and degrade Si anodes [6]. Details of this stress development are not well understood, although recently it was shown that particle size can play a significant role on stresses during elastic deformation

* Corresponding author. Tel.: +1 303 735 2103; fax: +1 303 492 4990.
E-mail address: maute@colorado.edu (K. Maute).

0378-7753/$ – see front matter © 2011 Elsevier B.V. All rights reserved.
doi:10.1016/j.jpowsour.2011.07.035

[10], and that inelastic deformation can occur [11,12] which influences the resulting stresses and thus probably fracture.

Numerous recent studies have shown that Si anodes with nm-scale morphologies are more resistant to mechanical degradation during Li insertion and cycling, and that this resistance depends significantly on the particle morphology. Li et al. [2] showed that anodes with Si particles ranging from 50 to 100 nm have better cycling performance than those with particles in the μm range. Chan et al. [1] showed that Si nanowires show better cycling performance than Si films or powders consisting of micrometer sized particles. Anodes made of structured arrays of Si nanotubes where electrochemical insertion reactions occur on the outer surface of the tube, but not on the inner surface, showed better cycling performance than anodes with either particle or nanowire architectures [3]. Kim et al. [4] fabricated nano-porous Si anodes with pore width and wall feature sizes in the range of 40–100 nm, and demonstrated that this architecture also exhibits better cycling performance than anodes with particle or nanowire architectures. These porous materials can be idealized as parts of thin spherical shells. The improvement from nanoscale architectures is related to the stresses developed during Li insertion, however a complete understanding of why particle size and morphology play such an important role is lacking. The goal of this paper is to contribute to a better understanding of the interaction between particle geometry and stresses by simulating the coupled diffusion and mechanics of Li insertion in Si as driven by electrochemical surface reactions.

While coupled species diffusion and mechanics has been studied for decades in many different contexts, only recently have analyses appeared for electrochemical insertion electrodes. Christensen and Neuman developed a fully-coupled diffusion-mechanics model to describe the behavior of spherical particles during insertion [13]. They then used this model to simulate stress generation and predict fracture in spherical $Li_yMn_2O_4$ particles [14]. Zhang et al. later developed a fully-coupled diffusion-mechanics model by treating diffusion induced strains analogously to thermal eigenstrains [15] and showed that their model provides more conservative estimates of stresses generated during insertion than the model proposed by Christensen and Neuman [13]. Zhang et al. studied Li insertion into Mn_2O_4 with the Li influx described by a constant current and through Butler–Volmer surface reaction kinetics [15,16]. In a series of recent papers Cheng and Verbrugge [17–19] provided valuable analytical solutions for the one-way-coupled diffusion induced stresses in particles for galvanostatic and potentiostatic driven insertion. They have also considered simplified surface reaction kinetics, modeling them as a convective boundary condition and introducing an electrochemical Biot number to classify the regimes where bulk diffusion or surface reactions dominate the process [19]. The latter is particularly valuable in understanding the roles of various parameters in the design of strain-resistant electrodes. Deshpande et al. studied the effects of surface stress [20] and concentration-dependent elastic constants [21] and showed that they can make a significant impact on stress development during potentiostatic or galvanostatic insertion. The latter study is especially timely as the dependence of elastic constants has recently been computed for Li–graphite and LiSi compounds using density functional theory [9,22]. Golmon et al. [10] used a fully-coupled diffusion-mechanics model with Li insertion driven by Butler–Volmer electrochemical reaction kinetics to study the effect of particle size on stress generation in Si particles. They developed a map that communicates the roles of particle size and Li insertion rate (related to charging rate in an actual battery) on the maximum stresses developed.

The studies outlined above have focused on stress generation during insertion/extraction with the understanding that stresses drive mechanical failure and damage. A few efforts have pursued more accurate failure criterion based on linear elastic fracture mechanics, which is appropriate given the brittleness of many of the insertion materials [23–31]. These studies have revealed the important roles of elastic anisotropy [31] and the nonuniform stress states that result during insertion [29].

In this paper we build on these previous modeling efforts and present a fully-coupled stress-diffusion model with electrochemical surface reactions at the electrode/electrolyte interface that incorporates surface stress [10,32–35] and concentration-dependent material properties. The model is presented in a general form amenable to a finite element formulation which can then be used to simulate arbitrary geometries. We use the model to simulate stresses during Li insertion in Si, focusing on two basic geometries: hollow spherical and cylindrical shells. These geometries are selected as they describe a wide variety of morphologies that have been fabricated and studied experimentally, including particles, nanowires, nanotubes, and porous solids. After studying the evolution of Li concentration and stresses during electrochemical insertion, we study the roles of surface stress and concentration-dependent elastic moduli for various particle sizes and morphologies. We then form parameter maps of the maximum stress components as functions of various parameters of relevance in the design of strain-tolerant electrodes.

2. Coupled stress-diffusion model

In general, during insertion (or extraction) ion transport occurs in both the active material and the surrounding electrolyte, coupled through electrochemical reactions at the particle surface. Here we idealize the situation and only consider transport and mechanics in the active host. The interaction with the electrolyte is modeled through a boundary condition on the particle surface that describes the Li ion flux into the particle in terms of the kinetics of the electrochemical charge-transfer reaction at the interface. In our model the electrolyte has a constant prescribed concentration of Li ions c_l and electric potential ϕ_l. The particle is assumed to be at a spatially constant potential, ϕ_s, and the potential difference, $\eta = \phi_l - \phi_s$, drives the electrochemical reaction kinetics, as discussed later. Fig. 1 illustrates the problem domain and the degrees of freedom of interest within each region.

Following Zhang et al. [15], we model the electrode particle as a linear elastic solid with diffusion-induced eigenstrains and extend that formulation to incorporate the effects of surface stress [33–35], which play an increasingly important role as feature sizes decrease to the nm scale. Assuming that the mechanical response is much faster than diffusion and neglecting body forces and inertia effects, deformation in the electrolyte is described by a linear

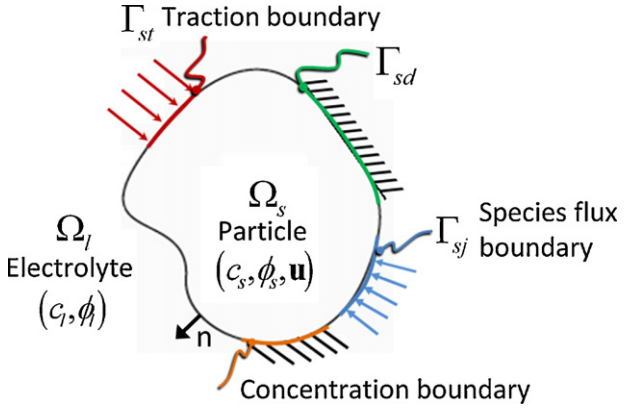

Fig. 1. Electrode particle.

elastic mechanical model, which can be written in weak form as:

$$\delta W_M = \int_{\Omega_s} \delta\boldsymbol{\varepsilon} : \boldsymbol{\sigma}\, d\Omega_s + \int_{\Gamma} \delta\boldsymbol{\varepsilon}_{\Gamma} : \boldsymbol{\tau}\, d\Gamma - \int_{\Gamma} \delta\mathbf{u}\cdot\mathbf{t}\, d\Gamma + \int_{\Omega_s} \delta\sigma_h \left(\sigma_h - \frac{tr(\boldsymbol{\sigma})}{3}\right) d\Omega_s = 0 \quad (1)$$

where Ω denotes the particle volume and Γ its surface; $\boldsymbol{\varepsilon}$ and $\boldsymbol{\sigma}$ are the strain and stress tensors. The first term accounts for bulk elasticity, and the second term accounts for surface stresses [33–35]; here the surface stress equilibrium equation [33] is presented in the weak form. The associated surface strain and stress tensors are denoted by ε_{Γ} and $\boldsymbol{\tau}$. The third term accounts for applied tractions $\mathbf{t}$ on the boundary. The fourth term arises because we treat the hydrostatic stress σ_h as an independent field to limit the computational expense needed in calculating the hydrostatic stress gradients.

Linear elastic constitutive relations connect the stress and strain, i.e. $\boldsymbol{\sigma} = \mathbf{C} : (\varepsilon - \varepsilon_{cs})$ and $\boldsymbol{\tau} = \boldsymbol{\tau}_0 + \mathbf{K}^s : \boldsymbol{\varepsilon}_{\Gamma}$, where $\mathbf{C}$ is the bulk elasticity tensor, $\boldsymbol{\tau}_0$ is the initial surface stress, and $\mathbf{K}^s$ is the surface elasticity tensor [34,36]. In general, $\mathbf{C}$ and $\mathbf{K}^s$ may be anisotropic; we assume isotropy in the numerical results we present. As we discuss in Section 4.3, the elastic tensor, $\mathbf{C}$, is either modeled as constant or as a function of the electrode concentration, c_s, to account for elastic stiffening or softening [9,21]. The chemical eigenstrain, $\boldsymbol{\varepsilon}_{cs}$, is calculated as $\boldsymbol{\varepsilon}_{cs} = c_s(\omega/3)\boldsymbol{\delta}$ where ω is the partial molar volume of Li in Si and $\boldsymbol{\delta}$ is the Kronecker delta. We assume infinitesimal strain and linear kinematics, i.e. $\boldsymbol{\varepsilon} = 1/2(\nabla\mathbf{u} + \nabla\mathbf{u}^T)$ and $\boldsymbol{\varepsilon}_{\Gamma} = 1/2(\nabla_{\Gamma}\mathbf{u} + \nabla_{\Gamma}\mathbf{u}^T)$ where $\mathbf{u}$ is the displacement vector, ∇ is the gradient operator, and ∇_{Γ} is the surface gradient operator defined by Gurtin and Murdoch [34].

Transport of Li ions in the electrode particle is modeled as a diffusive process:

$$\delta W_D = \int_{\Omega_s} \delta c_s \frac{\partial c_s}{\partial t} + \nabla\delta c_s \cdot \mathbf{j}\, d\Omega - \int_{\Gamma} \delta c_s\, \mathbf{j}\cdot\mathbf{n}\, d\Gamma = 0 \quad (2)$$

where c_s is the concentration of Li within the electrode, $\mathbf{j}$ is flux of Li within the electrode, and $\mathbf{n}$ is the electrode surface unit outward normal. Diffusive transport with stress-diffusion coupling arises through the elastic constitutive equations for the bulk and surface and also through the constitutive equation for Li flux, $\mathbf{j}$. $\mathbf{j} = \mathbf{D}(\nabla c_s - (\omega c_s/(RT))\nabla\sigma_h)$ where $\mathbf{D}$ is the diffusion coefficient tensor, R is the gas constant, and T is absolute temperature. In general, $\mathbf{D}$ can be anisotropic as well as a function of concentration; here we take $\mathbf{D}$ to be constant and isotropic. As a result our diffusion model does not contain an upper limit on concentration due to a stoichiometric maximum concentration. Recently Haftbaradaran et al. [37] remedied this limitation in the diffusion model; their model could be incorporated in our framework in a relatively straightforward manner.

In Eqs. (1) and (2), the displacement and concentration fields, $\mathbf{u}$ and c_s, respectively, are fully coupled: the Li concentration affects the mechanical response through the diffusion-induced strain $\boldsymbol{\varepsilon}_{cs} = c_s(\omega/3)\boldsymbol{\delta}$, and the diffusion response is coupled to the displacement field through the hydrostatic stress gradient $\nabla\sigma_h$. At the particle surface (the electrode/active material interface), Γ, we model the electrochemical charge-transfer reaction that balances the Li+ and Li fluxes and couples the potentials ϕ_l and ϕ_s. We use a Butler–Volmer [38,40] model to describe the reaction kinetics that lead to the surface current, $i_s = -(\mathbf{j}\cdot\mathbf{n})F$, and the resulting Li+/Li fluxes that depend on the Li+/Li concentrations and the electric potentials at Γ.

$$\begin{aligned} i_s &= i_0\left[\exp\left(\frac{\alpha_a F}{RT}(\eta - U(c_s))\right) - \exp\left(\frac{\alpha_c F}{RT}(U(c_s) - \eta)\right)\right] \\ i_0 &= Fk(c_{s\max} - c_s)^{\alpha_a} c_s^{\alpha_c} c_l^{\alpha_a} \\ \eta &= \phi_s - \phi_l \end{aligned} \quad (3)$$

F Faraday's constant, α_a, α_c are the anodic and cathodic transfer coefficients, respectively, $U(c_s)$ is the open circuit potential, and k is the reaction rate constant.

We use a finite element formulation of these basic equations that satisfies:

$$\delta W_M + \delta W_D = 0 \quad (4)$$

The finite element formulation can be derived with the standard Galerkin approach. In this study we consider solid and hollow, spherical and cylindrical particles. To efficiently analyze the spherical geometry, a one dimensional spherical element is formulated with the assumption that both the displacement and concentration fields are completely symmetric about both rotational axes in a spherical coordinate system with the origin placed at the center of the particle. With this assumption the only non-zero stress components are radial and tangential, and the only non-zero particle flux is in the radial direction. For a cylindrical geometry, a two dimensional axisymmetric element is formulated based on the assumption that both the displacement and concentration fields are completely symmetric about the z axis in a cylindrical coordinate system with the origin placed at the center of the particle. In the axisymmetric formulation, there are four nonzero stress components: radial, axial, hoop, and in-plane sheer stress. There is no out of plane Li flux in the axisymmetric formulation.

3. Simulation of Li insertion

We employ the finite element formulation of the coupled stress-diffusion model described in Section 2 to simulate the insertion of Li ions into Si particles of two general morphologies: spherical and cylindrical shells as illustrated in Fig. 2. Both geometries are characterized by two finite dimensions, outer and inner radii R_{out} and R_{in}, respectively; these give rise to a wall thickness $t = R_{\text{out}} - R_{\text{in}}$. Consistent with most fabricated nanowires and nanotubes with lengths much larger than their diameters, we model cylindrical shells as infinite in length. We realize solid spheres and cylinders by setting $R_{\text{in}} = 0$.

Spherical shells are discretized with 60 one-dimensional three-node elements and cylinders are discretized with eight-node quadrilateral elements, with 100 elements in the radial direction and two in the axial direction. The ends of the cylinders are constrained to remain on horizontal planes during deformation, with the use of multipoint constraints, so that the model represents an infinite cylinder.

For each particle we carry out simulations with electrochemical reactions (and thus Li insertion into silicon) on (i) the outer surface, and (ii) the inner and outer surfaces of the particle. This corresponds to various realizable experimental scenarios. For example, Song et al. [3] fabricated and tested Si nanotubes that were capped on the surfaces so that the electrochemical reactions only occurred on the outer surfaces; the inner surfaces of the nanotubes were isolated from an electrolyte. We assume that on each surface where reactions occur the ion concentration and potential fields in the electrolyte, c_l and ϕ_l, respectively, are uniform and prescribed at the values listed in the appendix.

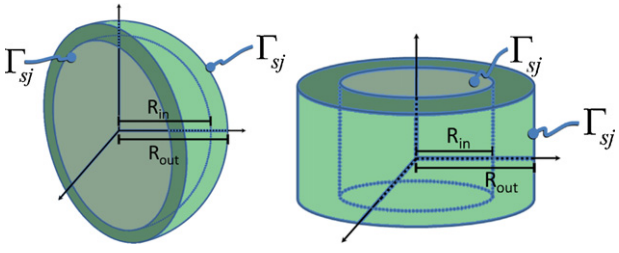

Fig. 2. Spherical and cylindrical particles.

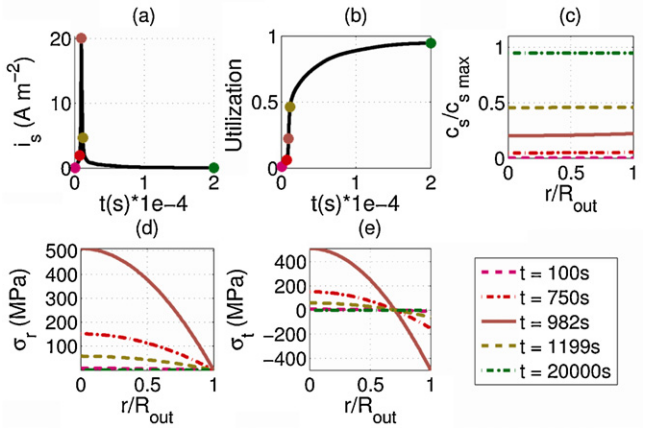

Fig. 3. Li insertion into a solid sphere (R_{out} = 1 μm): (a) current vs. time, (b) utilization vs. time, (c) normalized concentration profiles, (d) radial stress profiles, (e) tangential stress profiles. Colored dots on (a) and (b) correspond to times on legend.

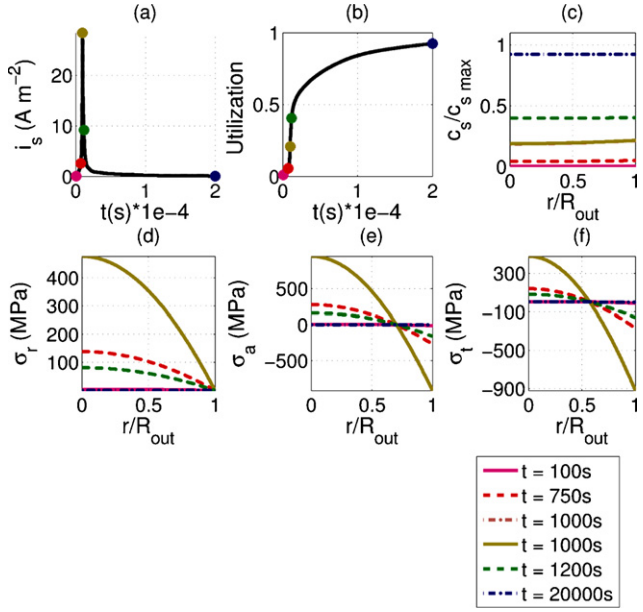

Fig. 4. Li insertion into a solid cylinder (R_{out} = 1 μm): (a) current vs. time, (b) utilization vs. time, (c) normalized concentration profiles, (d) radial stress profiles, (e) axial stress profiles, (f) tangential stress profiles. Colored dots on (a) and (b) correspond to times on legend.

The overpotential, $\eta = \phi_s - \phi_l$, drives the electrochemical reaction at the surface described by the Butler–Volmer Eq. (3) which results in Li flux. In our simulations we sweep the overpotential linearly according to $\eta = \phi_s - \phi_l = \eta_o - \beta t$ for $t \le t_s$, and then hold it constant at $\eta = \eta_o - \beta t_s$ for $t > t_s$ as described in Golmon et al. [10]. This type of simulation corresponds to a typical voltage sweep experiment. Here we use $\eta_o = U(c_o)$, $\beta = 0.91$ mV s^{-1}, $t_s = 1000$ s, and $c_0 = 0.01 c_{smax}$. Material properties and constants used in the simulations are presented in Appendix A. They are the same as those reported in Golmon et al. [10], except the initial surface stress and the surface elastic moduli are taken from Miller and Shenoy [39]. The open circuit potential of first insertion of Li ions into Si is interpolated from the experimental data [7].

4. Results and discussion

We present simulation results for Li ion insertion into spherical and cylindrical shell morphologies (Fig. 2) of varying sizes where the Li influx occurs either only on the outer surface or on both inner and outer surfaces. For each situation we consider three cases with regard to the influence of surface stress and concentration-dependent bulk elastic constants:

- Case 1: $\boldsymbol{\tau}_0 = \mathbf{K}^s = 0$; $\mathbf{C} \neq \mathbf{C}(c)$
- Case 2: $\boldsymbol{\tau}_0 \neq 0$; $\mathbf{K}^s \neq 0$; $\mathbf{C} \neq \mathbf{C}(c)$
- Case 3: $\boldsymbol{\tau}_0 = \mathbf{K}^s = 0$; $\mathbf{C} = \mathbf{C}(c)$

Case 1 can be considered our baseline case and cases 2 and 3 then explore the influence of surface elasticity and concentration-dependent elastic moduli, respectively. In the simulations our focus is on the evolution of the Li concentration profile through the particles over time and the resulting stress distributions. To assist in developing an understanding of the phenomena during Li insertion we first study the behavior in detail (current, concentration, utilization, and stress distributions) for solid spherical and cylindrical particles. Then we focus on the concentration and stress profiles at various times for the different geometries and each case listed above. Finally we study the maximum stresses that occur during Li insertion.

4.1. Stress-diffusion phenomena: case 1

Figs. 3 and 4 show the time dependence of the surface current and overall utilization (the average concentration of Li normalized by c_{smax}) as well as the spatial variation of Li concentration and the stress components at various times for 1 μm solid spherical and cylindrical particles, respectively. These geometries serve as a baseline for our subsequent studies of geometrical effects.

The qualitative behavior of both the spherical and cylindrical particles is the same; of course the cylindrical particle also has an axial stress component which behaves similarly to the tangential component. As the applied overpotential decreases linearly, the electrochemical reaction kinetics results in a rapidly increasing current influx that peaks at about 1000 s (the time after which the potential is held constant) and then drops quickly. This results in a rapid increase in utilization, followed by a continuing, but more gradual, increase after the current spike. The concentration profiles here are fairly flat, characteristic of surface reaction limited insertion, i.e. a low electrochemical Biot number [19]. For both geometries the radial stress σ_r is a maximum at the particle center and zero at the boundary (as prescribed) at all times. The distribution increases with time, peaks, and then decreases to zero over time as concentration gradients weaken. The tangential stress σ_t (and axial stress σ_a for the cylinder) is compressive at the surface and tensile at the center of the particle. All stress components peak at nearly the same time, just before the current peaks, and then decrease as Li is continually inserted. These results are consistent with similar ones recently reported in literature [10,16] and can physically be explained as follows. As Li is inserted, it first predominately fills an annular shell around the surface. If this shell were disconnected from the rest of the particle (the core) it would freely expand. Since the annular shell is connected to the core a mismatch strain exists that contracts the shell and stretches the core. As Li continues to diffuse into the particle the situation changes until at some point a nearly constant concentration distribution exists through the particle which generates no stress. Upon extraction, these trends are reversed. For spheres and infinite cylinders with equal radii, the radial stress is about the same, but the tangential stress on the surface is considerably higher for cylinders. The comparison of stress states for the same characteristic length, the radius, is probably not the most meaningful metric because the volume, and thus the amount of Li stored, is different in the two cases. We take up this issue in more detail in Section 4.4.

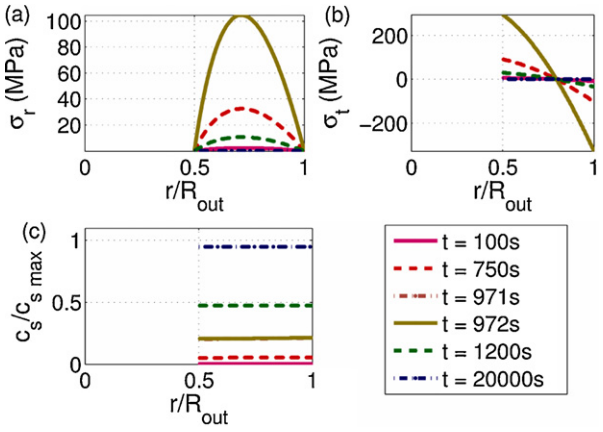

Fig. 5. Li insertion into the outer surface of a hollow sphere (R_{out} = 1 μm, R_{in} = 0.5 μm): (a) radial stress profiles, (b) tangential stress profiles, (c) normalized concentration profiles.

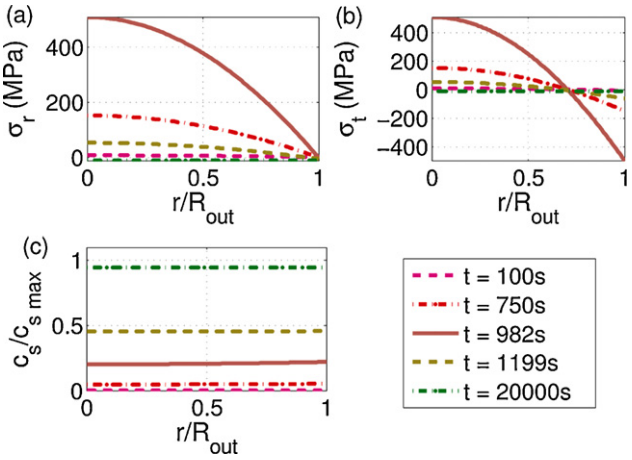

Fig. 7. Li insertion into a solid sphere with surface elasticity (R_{out} = 1 μm): (a) radial stress profiles, (b) tangential stress profiles, (c) normalized concentration profiles.

Figs. 5 and 6 show results for Li ion insertion into spherical shells with R_{out} = 1 μm and R_{in} = 0.5 μm.

In Fig. 5 Li insertion reactions occur only on the outer surface while in Fig. 6 they occur on both the outer and inner surfaces. Results for cylinders are qualitatively similar and thus are not shown. The concentration profiles for the hollow spheres, Figs. 5 and 6, are similar to those for solid particles in that they are fairly constant with position (at the resolution of the plot) as the insertion is again reaction dominated. Due to the free inner surface the radial stress is now zero at both surfaces during insertion and peaks at a position in the interior of the shell. The peak stress occurs at about the same time (near the current peak) for insertion on one or both surfaces. For the latter the radial position of the maximum radial stress is slightly shifted to the outside of the particle, but the radial stress distributions are quite similar. The main difference is that the magnitude of the peak radial stress is about twice as high for insertion on just the outer surface, although this value is about one-fifth of that for insertion into a solid particle. Comparing the three cases, the concentration gradients are lowest for the shell with insertion on both surfaces and highest for the solid sphere; this is the reason for the large difference in maximum stresses.

For the case with insertion on just the outer surface, the tangential stress distribution in the spherical shell is similar to that in the solid sphere, although the magnitude is about half of that for the solid sphere. In Fig. 5 the magnitude of the tangential stress is highest on the outer surface (where it is compressive), but there is a significant tensile tangential stress on the inner surface; this has implications for fracture initiation as surfaces often serve as sites for flaws that can propagate under tensile stresses. Insertion on both surfaces lowers the magnitude of the tangential stress but also qualitatively changes its distribution. As seen in Fig. 6 it now reaches a maximum in the shell interior and tends toward zero in the same manner as it does on the outer surface. While the numerical values of the stresses in Figs. 3, 5 and 6 depend on the actual geometrical parameters chosen, the qualitative results broadly persist and can be understood as the concentration gradients decrease with shorter distances for diffusion (shorter wall thickness) and insertion into both surfaces.

4.2. Stress-diffusion phenomena: case 2

To our knowledge, only Cheng and Verbugge [17] have considered the role of surface elasticity (surface stress and elastic constants) on diffusion-induced stresses in electrode particles, and their focus was on spherical particles subjected to potentiostatic and galvanostatic insertion. Since we are interested in the behavior of particles with nm-scale dimensions, partly due to the myriad studies that have demonstrated their superiority, it is important to understand the role of surface elasticity during Li insertion into Si particles. To this end Figs. 7–9 show results for Li insertion into solid spherical particles of three sizes: R_{out} = 1 μm,

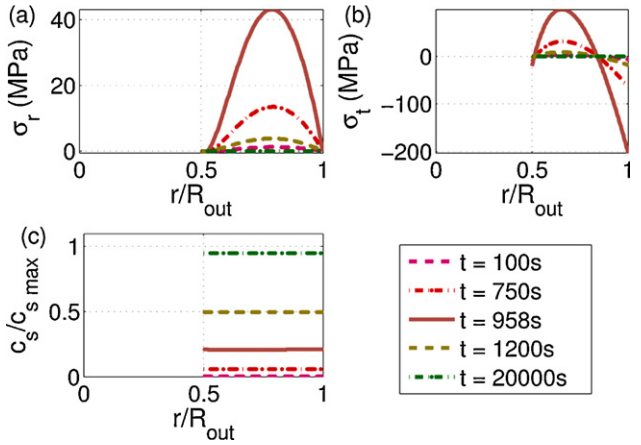

Fig. 6. Li insertion into both surfaces of a hollow sphere (R_{out} = 1 μm, R_{in} = 1 μm): (a) radial stress profiles, (b) tangential stress profiles, (c) normalized concentration profiles.

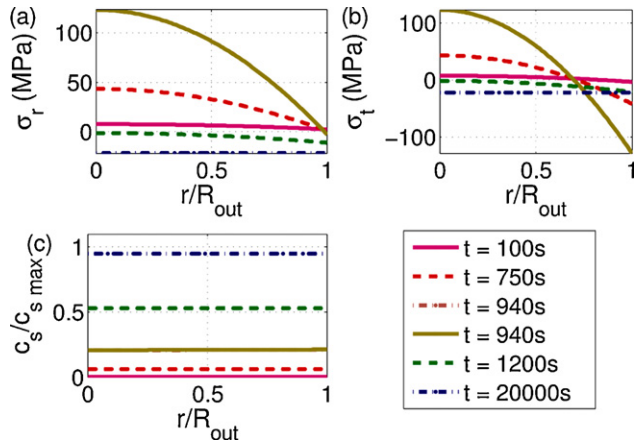

Fig. 8. Li insertion into a solid sphere with surface elasticity (R_{out} = 500 nm): (a) radial stress profiles, (b) tangential stress profiles, (c) normalized concentration profiles.

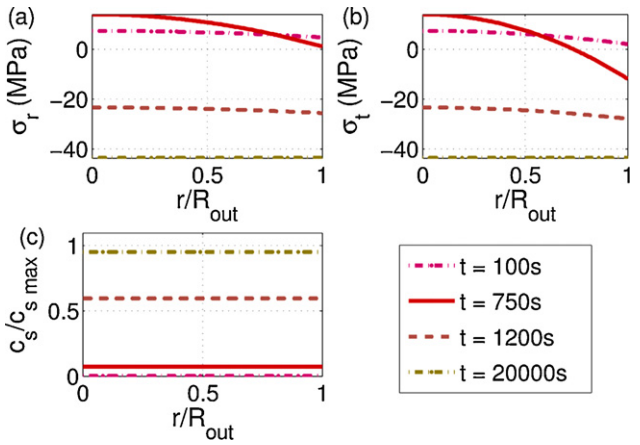

Fig. 9. Li insertion into a solid sphere with surface elasticity (R_{out} = 250 nm): (a) radial stress profiles, (b) tangential stress profiles, (c) normalized concentration profiles.

500 nm, and 250 nm. For the spherical Si particles, surface elasticity results in a radial pressure on the particle surface of magnitude $\sigma_r(R_o) = -(2/R_o)[\boldsymbol{\tau}_0 + \kappa^s(u_r(R_o)/R_o)]$ [17] that induces a stress field and adds to the diffusion-induced stresses. $\boldsymbol{\tau}_0$ is the initial surface stress and $\kappa^s = D_{11} + D_{12}$ is the surface elastic modulus.

The concentration and stress distributions for the 1 μm solid sphere (Fig. 7) are indistinguishable from those without surface elasticity (Fig. 1). The only notable difference is that the particle has a nonzero, but small, stress state at long times when the concentration gradients tend to zero. This is due to the tensile surface stress which induces a radial pressure of −10.8 MPa. Especially apparent is the large nonzero stress that exists at long times for smaller particles. In fact, the stresses due to surface elasticity can dominate the diffusion-induced stresses for smaller particles as shown (Fig. 9). The maximum tangential stresses (for all time) that occur in solid sphere particles during first insertion show the same behavior as the maximum radial stresses, so only the radial stresses are shown (Fig. 10). It is clear that without accounting for surface stress effects, smaller particles experience smaller stresses. However, if surface stresses are modeled, they dominate the maximum stresses experienced by particles smaller than ∼150 nm during first insertion.

Surface elasticity plays a more significant role for hollow particles because it acts on both surfaces. These effects are shown in Figs. 11–13. Fig. 11 shows the behavior of a particle (R_{out} = 1 μm, R_{in} = 0.5 μm) with Li insertion on only the outer surface, and Fig. 12 shows results for Li insertion on both the inner and outer surfaces. Again the free surfaces reduce the stresses as compared to the solid particles, and the surface elasticity influences the stress distribution more significantly, both qualitatively and quantitatively.

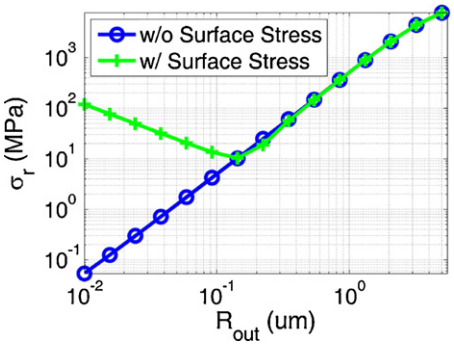

Fig. 10. Li insertion into solid spheres with and without surface elasticity: maximum radial stress during first insertion.

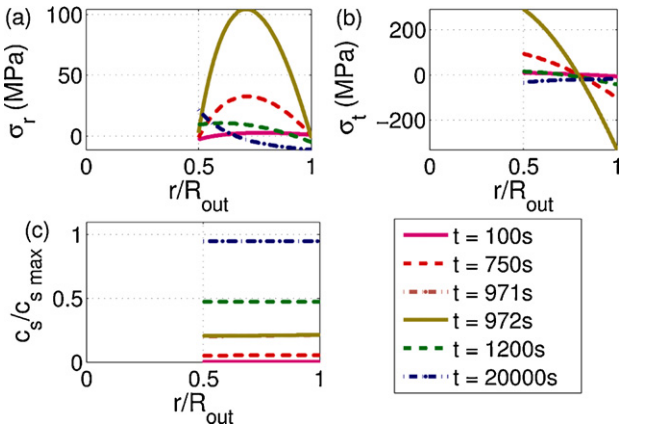

Fig. 11. Li insertion into the outer surface of a hollow sphere with surface elasticity (R_{out} = 1 μm, R_{in} = 0.5 μm): (a) radial stress profiles, (b) tangential stress profiles, (c) normalized concentration profiles.

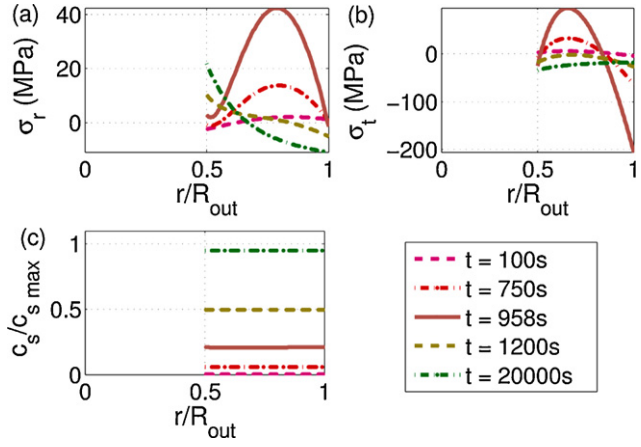

Fig. 12. Li insertion into both surfaces of a hollow sphere with surface elasticity (R_{out} = 1 μm, R_{in} = 0.5 μm): (a) radial stress profiles, (b) tangential stress profiles, (c) normalized concentration profiles.

As the size of the hollow particle decreases the influence of surface elasticity increase can be observed by comparing Figs. 11 and 13. Here the surface elasticity reduces the tangential stress component, but the maximum radial stress is greatly increased and continues to increase as the particle approaches full utilization. The radial stress takes on a maximum value at

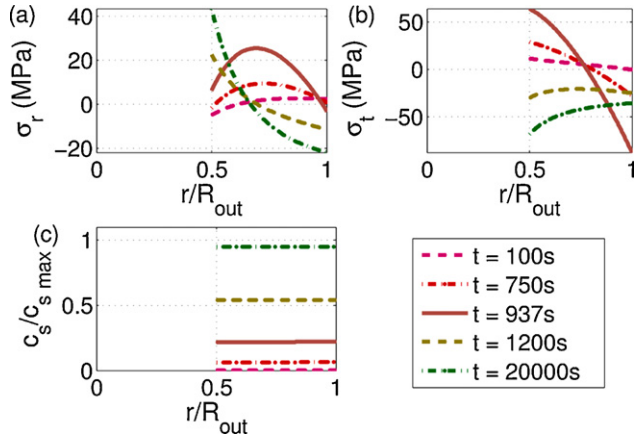

Fig. 13. Li insertion into the outer surface of a hollow sphere with surface elasticity (R_{out} = 1500 nm, R_{in} = 250 nm): (a) radial stress profiles, (b) tangential stress profiles, (c) normalized concentration profiles.

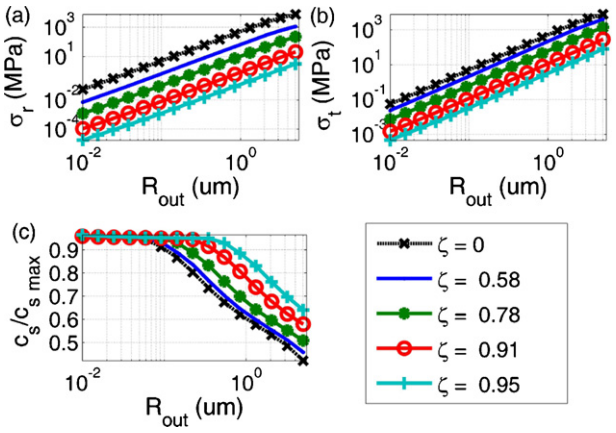

Fig. 14. Li insertion into the outer surface of spheres without surface elasticity ($R_{out} \in [0.01\ 5]$ μm and $\zeta \in [0\ 0.95]$): maximum (a) radial stress, (b) tangential stress, (c) and normalized concentration during first insertion.

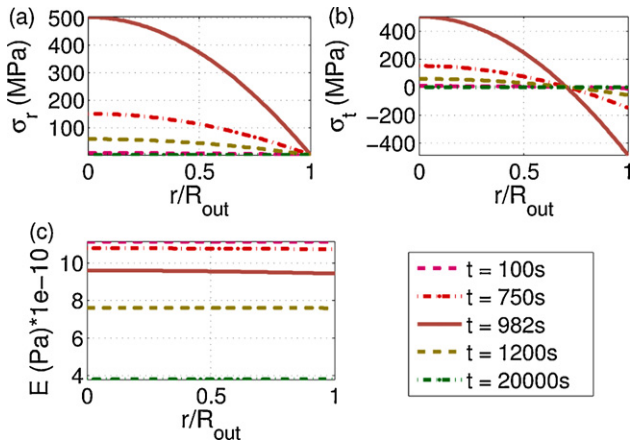

Fig. 16. Li insertion into a solid sphere with $E(c_s)$ ($R_{out} = 1$ μm): (a) radial stress profiles, (b) tangential stress profiles, (c) Young's modulus profiles.

the inner surface at full utilization. These results suggest that for nanoscale spherical shells, representative of electrodes fabricated from porous silicon, surface stress effects are particularly significant. Due to the high surface area to volume ratio, surface stresses can dominate the influence of the diffusion-induced stresses. This does not imply that the mechanics associated with diffusion is not important, though, because the deformation due to Li insertion alters the surface stresses increasing their significance when compared to the undeformed configuration.

It is clear that smaller particles are more significantly affected by surface elasticity than are larger particles. To better understand the influence of surface elasticity on particles of varying size and hollowness, a number of particles with and without surface elasticity with $R_{out} \in [0.01\ 5]$ μm and $\zeta \in [0\ 0.95]$ were simulated during first insertion, where the wall thickness ratio $\zeta = R_{in}/R_{out}$. The maximum radial and tangential stresses and the maximum normalized concentrations in each simulation are plotted in Figs. 14 and 15.

Fig. 14 shows that without surface elasticity maximum stresses decrease with decreasing R_{out}. These results are consistent with those reported by Golmon et al. [10]. It is clear from Fig. 14 that stresses also decrease with increasing wall thickness ratio, if surface elasticity is neglected. Smaller and more hollow particles experience smaller concentration gradients and thus smaller stresses. However, if surface elasticity effects are included this statement is generally not true. In small hollow particles which correspond to high surface area to volume ratios, maximum stresses are dominated by surface elasticity (Fig. 15). Therefore, surface elasticity should not be neglected when studying optimal electrode particle morphologies.

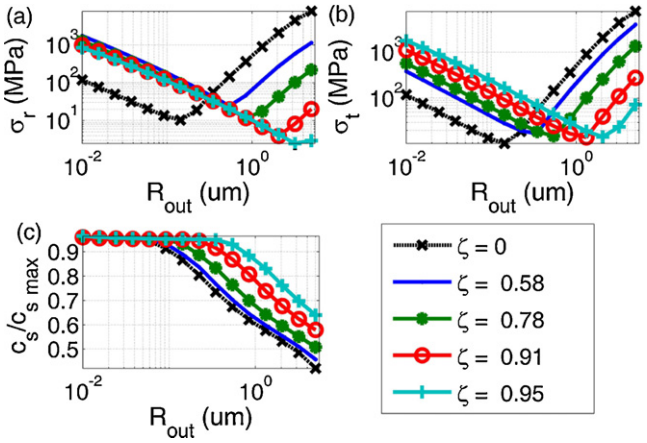

Fig. 15. Li insertion into the outer surface of spheres with surface elasticity ($R_{out} \in [0.01\ 5]$ μm and $\zeta \in [0\ 0.95]$): maximum (a) radial stress, (b) tangential stress, (c) and normalized concentration during first insertion.

4.3. Stress-diffusion phenomena: case 3

Deshpande et al. [21] recently studied the effects of concentration-dependent elastic moduli during potentiostatic insertion of Li into an infinite cylinder in the absence of stress-diffusion coupling. They considered both elastic stiffening and softening and found that the concentration-dependent moduli destroyed the symmetry of the stress state during insertion and extraction and had a significant effect on the stress evolution and peak stresses that resulted. Stiffening of the elastic moduli lowered the tensile stresses at the surface during extraction and softening lowered the tensile stresses at the core during insertion. Physically the latter occurs because as the outer part of the particle swells during insertion it softens, decreasing the stress due to the strain mismatch with radial position.

Elastic softening of Si due to Li insertion was shown recently by Shenoy et al. [9]. Using DFT simulations they studied the structure and elastic moduli of LiSi alloys and found that the polycrystal-averaged Young's modulus of amorphous Li_aSi_b decreased nearly linearly with composition from 90.13 GPa for Si to 18.90 GPa for Li, while Poisson's ratio decreased from about 0.28 to 0.24. The maximum concentration used in the simulations discussed in this paper is based on the assumption that the particle at full saturation is made up of $Li_{15}Si_4$ alloy. According to Shenoy et al. [9] amorphous $Li_{15}Si_4$ is ~30% as stiff as pure amorphous Li. To study the elastic softening effects of Si particles the Young's modulus is taken to vary as a linear function of the normalized Li concentration ($E(c_s) = E[1 - 0.7(c_s/c_{s\,max})]$), and the Poisson ratio was held constant. The Young's modulus and Poisson ratio used within are reported in the appendix. Figs. 16–18 show results for Li insertion into solid and hollow spherical particles with concentration-dependent Young's modulus and Butler–Volmer surface reaction kinetics. These plots are analogous to those in Figs. 3, 5 and 6 with constant Young's modulus.

Interestingly the elastic softening has almost no effect on the maximum stresses developed during Li insertion; the maximum stresses are decreased by <1.5%. While this appears to contradict the results reported by Deshpande et al. [21], the discrepancy is a result of the different boundary conditions (potentiostatic vs. reaction kinetics). Potentiostatic insertion models the case of a Si particle in an inexhaustible Li reservoir and prescribes a constant Li surface

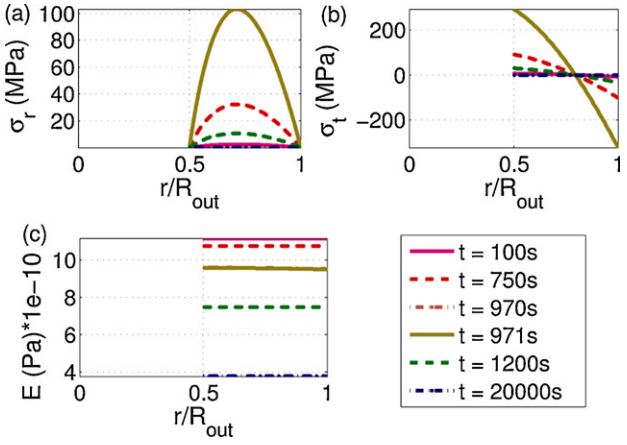

Fig. 17. Li insertion into the outer surface of a hollow sphere with $E(c_s)$ (R_{out} = 1 μm, R_{in} = 0.5 μm): (a) radial stress profiles, (b) tangential stress profiles, (c) Young's modulus profiles.

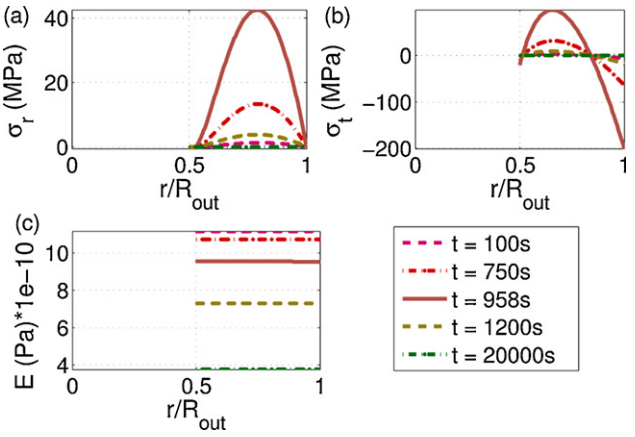

Fig. 18. Li insertion into both surfaces of a hollow sphere with $E(c_s)$ (R_{out} = 1 μm, R_{in} = 0.5 μm): (a) radial stress profiles, (b) tangential stress profiles, (c) Young's modulus profiles.

concentration. Physically this is most appropriate for diffusion-limited insertion. As described earlier, our situation is more akin to surface reaction limited insertion [19]. The concentration gradients are small and so the gradients in elastic constants are also small. This means the Young's modulus is nearly spatially constant in the particles even though it decreases with Li insertion. To make this clear we show plots of Young's modulus vs. position and time in Figs. 16–18 instead of concentration vs. position and time as we did in Figs. 3, 5 and 6. The results of Figs. 16–18 underscore the importance of accurately modeling the surface reaction kinetics.

4.4. Morphology effects

As we mentioned earlier, myriad experimental results have shown that particle size, charging/discharging rate, and morphology seem to impact the cycling performance, and this is presumably related to the stress state that develops. In this section we study the maximum stresses developed upon first insertion of Li in spherical and cylindrical solid and hollow Si particles. As silicon is brittle, we focus on the maximum tensile stresses. We note that if a more accurate fracture mechanics analysis is desired, the stress analysis presented here can serve to drive such an analysis as done by Woodford et al. [29]. While one can directly compare the stress state in different morphologies and sizes, this is probably not the most meaningful comparison because even though stresses may be low, it may be at the expense of reduced Li inserted, and thus capacity.

We provide a basis for comparing the different morphologies by introducing two parameters of practical relevance: foot print volume, V_{FP}, and capacity ratio, C_{ap}. $V_{FP} = (4/3)\pi R_{out}^3$ and $C_{ap} = 1 - \zeta^3$ for spheres and $C_{ap} = 1 - \zeta^2$ for cylinders. The foot print volume is the volume of a solid spherical particle, or a solid cylindrical particle with length $l = (4/3)R_{out}$. The foot print volume includes the empty volume inside of hollow particles. The cylinder length is chosen such that spheres and cylinders with the same R_{out} have the same foot print volume. The capacity ratio is the fraction of a single particle that contains electrode material, therefore $V_{FP}C_{ap}$ is the material volume of a single electrode particle.

We study a range of particle sizes and geometries by simulating numerous spherical and cylindrical particles with $R_{out} \in [0.01\ 5]$ μm and $\zeta \in [0\ 0.95]$; the latter covers the range from solid particles to those with thin shells. During each insertion simulation we recorded the maximum tensile stress experienced by the particle. We only present results for the cases with surface stress included, but later comment on the behavior when surface stress is absent. As discussed in the previous section, in all morphologies and sizes, the stresses vary with both position and time, and each particle experiences different stress distributions. In order to identify optimal particle geometries, maximum stress component contours are plotted on a map defined by the foot print volume, V_{FP}, and capacity ratio, C_{ap}.

Fig. 19 shows the maximum stresses with Li insertion into only the outer surface of spherical particles, and Fig. 20 shows similar results with insertion on both the inner and outer surface. Figs. 21 and 22 then show companion results for cylindrical particles. For a specified capacity ratio, the maximum stress decreases with particle size (volume in the figures) for both spheres and cylinders, but reaches a minimum and then increases as the particle size continues to decrease. This is due to the interplay of reaction kinetics and diffusion as particle sizes decrease followed by an increasing influence of surface stresses as particle sizes continue to decrease

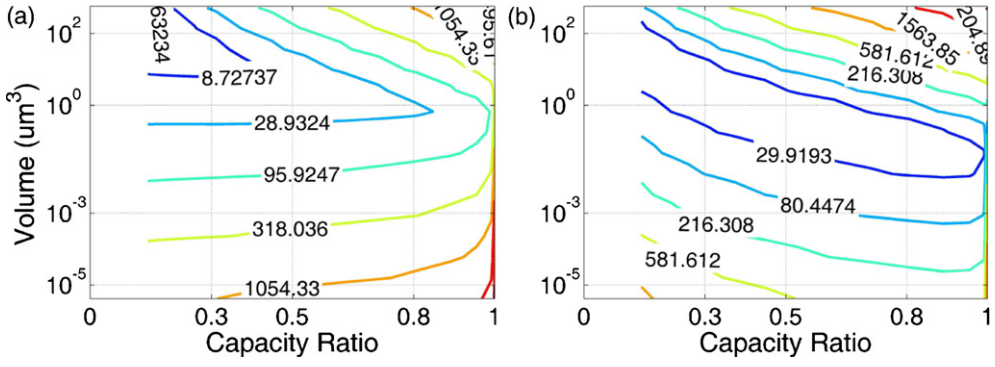

Fig. 19. Stress in (MPa): maximum (a) radial and (b) tangential stress during Li insertion into only the outer surface of spherical particle.

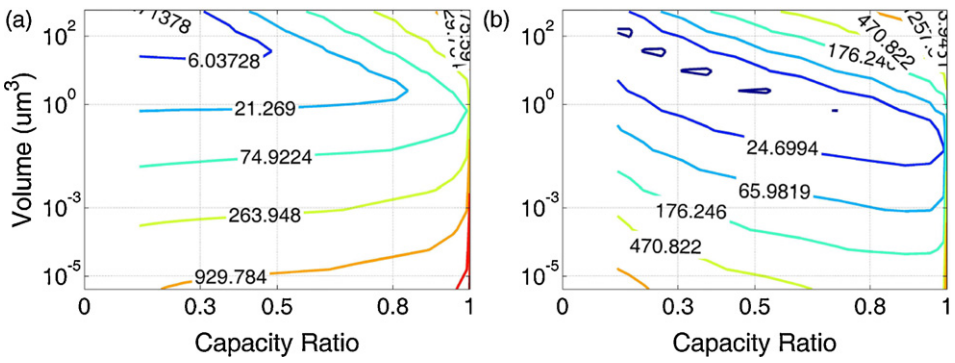

Fig. 20. Stress in (MPa): maximum (a) radial and (b) tangential stress during Li insertion into both surfaces of spherical particles.

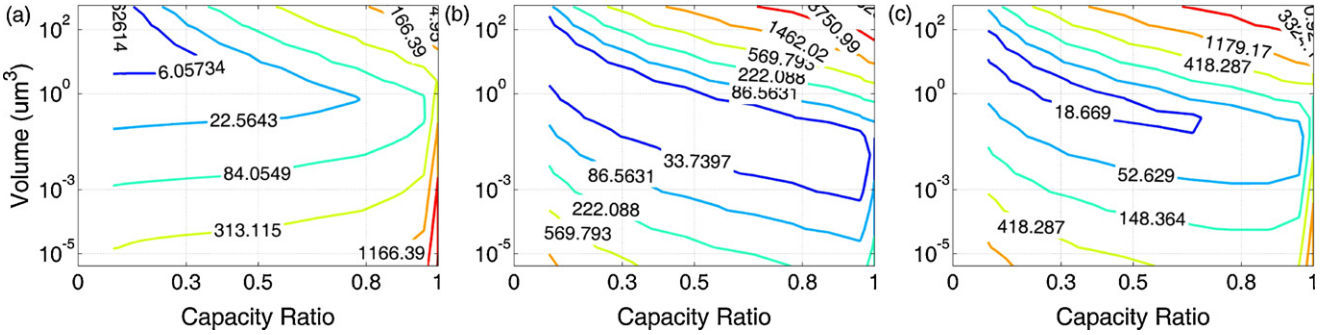

Fig. 21. Stress in (MPa): maximum (a) radial, (b) axial, and (c) tangential stress during Li insertion into only the outer surface of cylindrical particles.

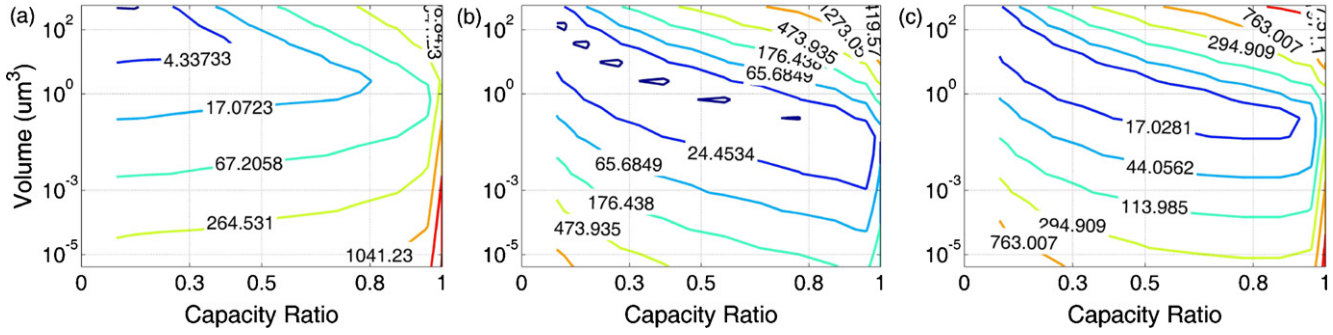

Fig. 22. Stress in (MPa): maximum (a) radial, (b) axial, and (c) tangential stress during Li insertion into both surfaces of cylindrical particles.

to the nm-scale. The results also show a similar trend to decreasing capacity ratio with a constant particle size. This is because the surface area to volume ratios increase and diffusion lengths decrease as capacity ratios decrease. This gives rise to lower concentration gradients which result in smaller stresses. For the same reason, the stresses are lower in the case where Li insertion occurs on both the inner and outer surfaces. Although, for very small capacity ratios the surface area to volume ratio is large enough that surface elasticity dominates the maximum stresses. The appearance of an optimum (minimum) in stresses has important implications for the design of damage-tolerant electrodes.

In comparing the results in Figs. 19–22 it is evident that the difference in stress magnitudes is not dramatically different for spherical and cylindrical particles. The results agree with the experimental observation that particles with diffusion distances on the order of 100 nm demonstrate better cycling performance than those with larger diffusion distances [1–4], although the authors have found no published results of experiments with small enough particles to observe the theoretical decrease in performance for smaller diffusion distances.

5. Summary and conclusions

We studied the effects of particle morphology and size on stress generation during Li insertion into Si particles using a fully coupled diffusion-elasticity model implemented in a finite element formulation. The model includes the effects of electrochemical reaction kinetics through a Butler–Volmer equation, concentration-dependent material properties, and surface stresses.

Stresses generated during Li insertion generally decrease as particles decrease from the μm-scale, reaching a minimum at the nm-scale. The minimum occurs at larger particle sizes for increasingly hollow particles. Surface stresses then begin to dominate the mechanical behavior as the particle size continues to decrease, resulting in an increase in stresses. It was demonstrated that there is a range of optimal Si particle sizes with respect to stresses. The existence of an optimum particle size has implications for the design of durable electrodes. Due to the shorter diffusion distances, hollow particles experience lower stresses than solid ones, while particles with surface fluxes on both inner and outer surfaces experience smaller stresses due to the increase in Li influx surface area. The

lower stresses states come at the expense of capacity. However, there is not a significant difference in magnitude between the maximum stresses for spherical and cylindrical particles. Based on the claims by Chan et al. [1], the authors expected to determine that cylinders are superior to spheres, but the results of the studies presented suggest that this is not the case for unconstrained particles. While concentration-dependent elastic softening of Si can significantly influence stress generation for potentiostatic insertion, its' role is not significant when more realistic electrochemical surface reaction kinetics are considered.

These results illuminate many important aspects of stress generation in Si electrodes. However, our model is built upon a few simplifications which need to be considered when interpreting the simulation results: (i) although the electrochemical eigenstrains of Si are large, we assume linear kinematics and elastic material behavior; both assumptions can be relaxed in more sophisticated treatments and are being pursued by the research community that consider geometric nonlinearity, phase transformations, and plastic deformation; (ii) while our modeling framework can accommodate anisotropic nonlinear behavior, we assume isotropy and consider only a simple dependency of the Young's modulus on the Lithium concentration in our simulations, and (iii) our model does not account for transport phenomena within the electrolyte but assumes a constant Lithium concentration and electric field in the electrolyte surrounding the particle. Therefore, the influence of the particle morphology and the associated spatial arrangements of particles on the Lithium transport in the electrode is neglected; (iv) we do not consider a failure criterion for the Si particles, but just compute the stresses that are generated. An appropriate failure criterion will have to be coupled with the stress analysis to achieve high-fidelity predictions of particle fracture.

Appendix A.

Material properties and constants.

Symbol	Name	Value
E	Young's modulus of elasticity	1.124e11 Pa
ν	Poisson ratio	0.28
$\boldsymbol{\tau}_0$	Initial surface stress	$-0.6505\,\mathrm{N\,m^{-1}}$
D_{11}	Surface elastic constant 1	$10.65\,\mathrm{N\,m^{-1}}$
D_{12}	Surface elastic constant 2	$3.888\,\mathrm{N\,m^{-1}}$
ρ	Density	$2.33\,\mathrm{g\,cm^{-3}}$
ω	Partial molar volume	$4.265\mathrm{e}{-6}\,\mathrm{m^3\,mol^{-1}}$
D	Diffusion coefficient	$1.0\mathrm{e}{-15}\,\mathrm{m^2\,s^{-1}}$
k	Surface reaction rate constant	$1.0\mathrm{e}-13\,\mathrm{m^{5/2}\,mol^{-1/2}\,s^{-1}}$
$c_{s\max}$	Max electrode Li concentration	$311,053\,\mathrm{mol\ m^{-3}}$
c_l	Electroltye Li concentration	$1000\,\mathrm{mol\ m^{-3}}$
ϕ_l	Electroltye potential	0 V
T	Temperature	300 K
$U'(c_s)$	Open circuit potential	Bagetto et al. [7]
R	Gas constant	$8.314\,\mathrm{J\ K^{-1}\,mol^{-1}}$
F	Faraday's constant	$96,487\,\mathrm{C\ mol^{-1}}$
α_a	Anodic transfer coefficient	0.5
α_c	Cathodic transfer coefficient	0.5

References

[1] C.K. Chan, H. Peng, G. Liu, K. McIlwrath, X.F. Zhang, R.A. Huggins, Y. Cui, Nat. Nanotechnol. 3 (2008) 31.
[2] H. Li, X. Huang, L. Chen, Z. Wu, Y. Liang, Electrochem. Solid-State Lett. 2 (1999) 547.
[3] T. Song, J. Xia, J.-H. Lee, D.H. Lee, M.-S. Kwon, J.-M. Choi, J. Wu, S.K. Doo, H. Chang, W.I. Park, D.S. Zhang, H. Kim, Y. Huang, K.-C. Hwang, J.A. Rogers, U. Paik, Nano Lett. 10 (2010) 1710.
[4] H. Kim, B. Han, J. Choo, J. Cho, Angew. Chem. Int. Ed. 47 (2008) 10151.
[5] M. Green, E. Fielder, B. Scrosati, M. Wachtler, J.S. Moreno, Electrochem. Solid-State Lett. 6 (2003) A75.
[6] U. Kasavajjula, C. Wang, A.J. Appleby, J. Power Sources 163 (2007) 1003.
[7] L. Baggetto, R.A.H. Niessen, F. Roozeboom, P.H.L. Notten, Adv. Funct. Mater. 18 (2008) 1057.
[8] B.A. Boukamp, G.C. Lesh, R.A. Huggins, J. Electrochem. Soc. 128 (1981) 725.
[9] V.B. Shenoy, P. Johari, Y. Qi, J. Power Sources 195 (2010) 6825.
[10] S. Golmon, K. Maute, S.-H. Lee, M.L. Dunn, Appl. Phys. Lett. 97 (2010) 033111.
[11] V.A. Sethuraman, M.J. Chon, M. Shimshak, V. Srinicasan, P.R. Guduru, J. Power Sources 195 (2010) 5062.
[12] K. Zhao, M. Pharr, J. Vlassak, Z. Suo, J. Appl. Phys. 109 (2011) 016110.
[13] J. Christensen, J. Newman, J. Solid State Electrochem. 10 (2006) 293.
[14] J. Christensen, J. Newman, J. Electrochem. Soc. 153 (2006) A1019.
[15] X. Zhang, W. Shyy, A.M. Sastry, J. Electrochem. Soc. 154 (2007) A910.
[16] X. Zhang, A.M. Sastry, W. Shyy, J. Electrochem. Soc. 155 (2008) 542.
[17] Y.-T. Cheng, M.W. Verbrugge, J. Appl. Phys. 104 (2008) 083521.
[18] Y.-T. Cheng, M.W. Verbrugge, J. Power Sources 190 (2009) 453.
[19] Y.-T. Cheng, M.W. Verbrugge, J. Electrochem. Soc. 157 (2010) A508.
[20] R. Deshpande, Y.-T. Cheng, M.W. Verbrugge, J. Power Sources 195 (2010) 5081.
[21] R. Deshpande, Y. Qi, Y.-T. Cheng, J. Electrochem. Soc. 157 (2010) A967.
[22] Y. Qi, H. Gou, L.G. Hector, A. Timmons, J. Electrochem. Soc. 157 (2010) A558.
[23] R. Huggins, W. Nix, Ionics 6 (2000) 57.
[24] K.E. Aifantis, S.A. Hackney, J. Mech. Behav. Mater. 14 (2003) 413.
[25] K.E. Aifantis, J.P. Dempsey, J. Power Sources 143 (2005) 203.
[26] K.E. Aifantis, J.P. Dempsey, S.A. Hackney, Rev. Adv. Mater. Sci. 10 (2005) 403.
[27] K.E. Aifantis, S.A. Hackney, J.P. Dempsey, J. Power Sources 165 (2007) 874.
[28] T.K. Bhandakkar, H. Gao, Int. J. Solids Structures 47 (2010) 1424.
[29] W.H. Woodford, T.-M. Chiang, W.C. Carter, J. Electrochem. Soc. 157 (2010) A1052.
[30] Y.-T. Cheng, M.W. Verbrugge, Electrochem. Solid-State Lett. 13 (2010) A128.
[31] Y. Hu, X. Zhao, Z. Suo, J. Mater. Res. 25 (2010) 1007.
[32] S. Golmon, K. Maute, M.L. Dunn, Comput. Struct. 87 (2009) 1567.
[33] M.E. Gurtin, A.I. Murdoch, Arch. Ration. Mech. Anal. 57 (1975) 291.
[34] M.E. Gurtin, A.I. Murdoch, Int. J. Solids Struct. 14 (1978) 431.
[35] P. Sharma, S. Ganti, N. Bhate, Appl. Phys. Lett. 82 (2003) 535.
[36] A. Ricci, C. Ricciardi, Sens. Actuators A 159 (2010) 141.
[37] H. Haftbaradaran, J. Song, W.A. Curtin, H. Gao, J. Power Sources 196 (2011) 361.
[38] D. Zhang, B.N. Popov, R.E. White, J. Electrochem. Soc. 147 (2000) 831.
[39] R.E. Miller, V.B. Shenoy, Nat. Nanotechnol. 11 (2000) 139.
[40] A.J. Bard, L.R. Faulkner, Electrochemical Methods , 2nd ed., Wiley, New York, 2001.